Journal of Applied Polymer Science

Rational design and preparation of dibenzothiophene-targeting molecularly imprinted polymers with molecular dynamics approaches and surface-initiated activators regenerated by electron-transfer atom-transfer radical polymerization

Chunxiao Qiu, Wenming Yang, Zhiping Zhou, Yongsheng Yan, Wanzhen Xu
School of Material Science and Engineering, Jiangsu University, Zhenjiang 212013 China
Correspondence to: Z. Zhiping (E-mail: zhouzp@ujs.edu.cn)

ABSTRACT: Nine molecular dynamic simulations of molecular-imprinting prepolymerization systems were performed to investigate the effects of the type and concentration of crosslinkers (CLs) on key template (T)–functional monomer (FM) complexes. Subsequent analyses revealed that the system with divinylbenzene as the CL had the most stable T–FM complexes, and the mass percentage concentration of divinylbenzene in the prepolymerization system was 9.4%. Nine corresponding imprinted polymers were synthesized by the coupling of the surface-initiated activator regenerated by electron-transfer atom-transfer radical polymerization technique with the hierarchical-imprinting technique to validate the reliability of the simulation results. The structural properties of the optimal adsorbent were characterized by IR spectrophotometry, scanning electron microscopy, and nitrogen sorption measurements. The Langmuir isotherm fitted the equilibrium data best, and the kinetic data (within 30 min) were well described by the pseudo-second-order model. Meanwhile, the prepared adsorbent displayed a higher selectivity to dibenzothiophene compared with other analogs. Finally, the adsorbent was successfully applied for the deep desulfurization of the gasoline sample. © 2015 Wiley Periodicals, Inc. J. Appl. Polym. Sci. **2015**, *132*, 42629.

KEYWORDS: adsorption; amorphous; applications; copolymers; molecular recognition

Received 8 December 2014; accepted 16 June 2015
DOI: 10.1002/app.42629

INTRODUCTION

Molecular imprinting is a versatile technique that is used to create binding sites within a network polymer and is potentially complementary to a preselected template in size, shape, and functionality.[1–5] Because of its synthetic efficiency and low cost, this technique has become a powerful alternative for the selective enrichment and separation of chemical species.[6–8] Despite the fact that various imprinted materials were made, many challenges still remain to be addressed.

One recurring problem in recognition-based applications of molecular imprinting is the low yield of high-affinity sites. In many cases, the imprinting process proceeds with low fidelity.[9,10] As a result, a large excess of functional monomer (FM) is often used to ensure the formation of key template (T)–FM clusters; this gives rise to a high percentage of background sites that possess low affinity and selectivity for the guest molecule. Many studies have aimed to improve the ratio of high-affinity to low-affinity binding sites; they have included the stoichiometric imprinting strategy,[11,12] covalent imprinting mechanisms,[13] and site-selective chemical modification of molecularly imprinted polymers (MIPs).[14] A defect common to all of these approaches is that the best results for MIP formulation need to be determined by empirical optimization via additional synthetic steps. These time-consuming processes diminish one of the primary advantages of molecular-imprinting technology, that is, the synthetic efficiency; therefore, they inhibit the widespread applications of MIPs.[15] Recently, Zhang *et al.*[9] demonstrated that FM dimerization could effectively reduce the number of background sites in both experiments and simulation. Although the monomer dimerization can actually improve the imprinting efficiency, it also reduces the number of templated sites, sacrificing part of the absorption capacity. In our group, computational chemistry was introduced to MIP design to prevent an FM overdose.[16–18] For example, the restricted Hartree–Fock (RHF) method at the 6–311G level was used to determine the minimum energy conformation of complex systems formed by indole and monomers [4-vinylpyridine (4-VP), Acrylamide (AM), and methacrylic acid (MAA)]. The performance of the as-prepared denitrogenation adsorbents was greatly enhanced in terms of the selectivity and adsorption capacity. In some circumstances, the choice of the crosslinker may also affect the formation of high-affinity binding sites. Mosbach *et al.*[19] prepared a series of imprinted polymers containing different combinations of FM and crosslinker to

research the effect of the crosslinker on the binding characteristics of the synthetic polymer, from which they drew the conclusion that polymers containing divinylbenzene (DVB) showed better binding capacities and higher selectivities toward the template.[19] Nevertheless, in our previous theoretical analyses of the prepolymerization mixture, the influences of the solvent and crosslinker (CL) on the stability of the T–FM clusters formed in the candidate molecular-imprinting prepolymerization systems were generally not considered.

Another problem is the incompatibility between the conditions that are optimal for creating the template binding sites at a molecular level with those leading to a predefined morphology at the microlevel.[20–22] Surface-initiated living radical polymerization (SILPR) combined with hierarchical imprinting is thus proposed to circumvent the problem. SILPR has been rapidly developing because of its excellent controllability on the thickness and uniformity of the coated polymer film.[23,24] Great efforts have been made to tailor silica particle surfaces with the polymer shell by SILPR, most notably, atom-transfer radical polymerization (ATRP). ATRP, one of living polymerization technique, has been widely used for the synthesis of polymers with a desirable molecular architecture and for the preparation of various advanced materials.[25,26] We recently reported the preparation of several MIP composite materials for oil treatment based on surface-initiated ATRP.[27–29] Activator regenerated by electron-transfer (ARGET) ATRP, a recent ATRP variant, is advantageous over conventional ATRP because of enhanced oxygen tolerance to the reaction and significantly reduced copper catalyst concentration (down to parts per million levels).[30,31] These advantages make the application of SILPR simpler in practice. Through hierarchical imprinting, one can simultaneously obtain a homogeneous polymer coating that exhibits molecular recognition properties on the mold and imprinted polymer beads with a desirable morphology.[32]

With greater attention given to environmental protection, organosulfur standards for transportation fuels are more strict. Conventional desulfurization technologies, such as hydrodesulfurization, oxidative desulfurization, catalyst desulfurization, and biological desulfurization, have not satisfied refineries' requirements in the deep desulfurization field.[33–36] Our research group has developed several adsorbents with high recognition selectivity and binding affinity to dibenzothiophene (DBT) over structure analogs, and batch adsorption studies were carried out to investigate their adsorption behaviors.[28,29,37–46] For instance, a computational simulation method was introduced to simulate the interactions between DBT and FMs in the prepolymerization mixture. On the basis of the simulation and analysis results, a novel DBT-imprinted polymer with a favorable performance was prepared by the surface-imprinting technique combined with controllable living radical polymerization; this provides another choice in the deep desulfurization field.

Herein, a comprehensive theoretical analysis of the various interactions existing in the prepolymerization solution was undertaken; we aimed to design an optimal quantitative relation of templates, FMs, and crosslinking agents. Then, a novel class of DBT-imprinted polymers was prepared by the combination of hierarchical-imprinting and surface-initiated ARGET ATRP. The analyses regarding the structures and adsorption performance of the adsorbents were subsequently presented. Finally, the as-prepared polymers were successfully applied for the desulfurization of the real sample.

EXPERIMENTAL

Materials

Benzothiophene (BT; 99%), DBT (98%), 4-methyl benzothiophene (4-MDBT), 4,6-dimethyldibenzothiophene (4,6-DMDBT), MAA, copper(II) bromide ($CuBr_2$), teradecane, triethylamine (TEA), 2-Bromoisobutyryl bromide, 3-aminopropyltriethoxysilane, glycerol dimethacrylate (GDMA), DVB, and ethylene glycol dimethacrylate (EDMA) were supplied by Sigma-Aldrich Chemical Co. (St. Louis, MO). EDMA was purified by washing in sequence with 10% aqueous NaOH, water, brine, and water. After drying over $MgSO_4$, pure EDMA was obtained by distillation *in vacuo*. DVB and GDMA were purified by the same procedure. MAA was purified by distillation *in vacuo* before use. Methanol, acetic acid, toluene, *n*-octane, acetone, acetonitrile, aqueous ammonia (25%), and tetraethoxysilane were obtained from Sinopharm Chemical Reagent (Shanghai, China). Tris[2-(dimethyamino)ethyl] amine (Me_6TREN) was synthesized by a one-step synthetic procedure from commercially available tri(2-aminoehyl)amine (Acros; 97%) according to the reported procedure.[47] All of these chemicals were analytical or high performance liquid chromatography grade and were used as received unless stated otherwise.

Instruments and Characterization

The Brunauer-Emmett-Teller surface area of the prepared nanoparticles was measured on a Micromeritics FlowsorbII2300 instrument with nitrogen adsorption at 77 K. Fourier transform infrared spectra (4000–400 cm^{-1}) in KBr was recorded on a Nicolet Nexus 470 Fourier transform infrared spectroscopy (Thermoelectric). The morphology and microstructure of the initiator-modified silica supports and silica-based imprinted polymer were characterized by JEM-2100 (high resolution) transmission electron microscopy (Japan Electron Optics Laboratory co., Japan). The samples for transmission electron microscopy were obtained by the placement of a drop of a dilute ethanol dispersion of nanoparticles on the surface of a copper grid.

Molecular Dynamics Simulations

All-atom molecular dynamic simulations were performed with the Materials Studio 7.0 suite of programs (Accelrys, Inc., San Diego, CA). We began the preparation of a simulation by inputting the chemical structures of DBT, MAA, DVB, and toluene into Materials Studio. The energies of DBT, MAA, DVB, and toluene were subsequently minimized, respectively. Minimization was performed with 10,000 smart minimizer steps by the discover module.

A box was constructed to study the monomer–template complexes in the prepolymerization solution by the amorphous module at 298 K and 1 bar, and the periodic boundary condition was applied in all three directions.[48,49] Certain amounts of DBT, MAA, DVB, and toluene were added to the box according to the system composition (see Table I). We estimated the initial box dimensions by considering the molecular weight and density of each of the components of the mixture. The target density of the final configurations was set at 0.87 g/cm^3. Then,

mixtures in the cubic simulation box were energy minimized with 10,000 smart minimization steps.

After these energy minimization procedures, isothermal equilibration at constant volume was performed at 298 K for 200 ps. The temperature was subsequently increased to 698 K, and we repeated the previous operation for 200 ps. The complete relaxation of the prepolymerization system occurred. Then, MD simulation was performed in the cannonical ensemble ensemble at 298 K for 200 ps. After that, we executed the annealing process from 298 to 698 K at a constant volume by implementing a Forcite module. Finally, isothermal equilibration was performed for 200 ps with a pressure of 1 bar and a temperature of 298 K. The production phase trajectory data was then collected.

In this study, a Condensed-phase Optimized Molecular Potential for Atomistic Simulation Studies force field was used throughout the simulation.[50,51] The nonbonded interactions were performed with the atom-based cutoff of 9.5 Å, a spline width of 1.0 Å, and a buffer width of 0.5 Å. The temperature was maintained via the Andersen method, and the pressure was held constant with the Berendsen method. The time for each dynamics step was 1 fs. Frames were outputted every 100 steps. The final production phase trajectories were analyzed by the implementation of the Forcite analysis tool.

Radial distribution functions (RDFs) were proposed to quantify the local densities of specified atom pairs at the optimal distance for interaction. This could be expressed by the following equation:

$$g(r)=\frac{\rho_{ir}(r)}{\rho_r} \quad (1)$$

where ρ_{ij} and $<\rho_r>$ are the observed number density of a specified solvent atom at a certain distance (r) from a solute atom (i) and the average bulk atom number density of the solvent, respectively.

Preparation and Modification of the Silica Supports

Uniform silica particles were synthesized by the Stöber method.[52] Ammonium hydroxide (28%, 2.0 mL) was added to anhydrous ethanol (20 mL). Tetraethoxysilane (1 mL) was added, and the mixture was stirred for 24 h. To modify the silica surface with amino groups, 3-aminopropyltriethoxysilane (0.05 mL) was added to the previous solution and stirred for another 24 h. After the reaction, the prepared sample was centrifuged at 10,000 rpm for 10 min to collect the silica cores. The cores were further washed with ethanol and double-deionized water by centrifugation several times to remove the unreacted chemicals. The obtained light yellow amino-modified cores was finally dried in a vacuum oven at 60°C for 1 day.

Immobilization of the ATRP Agent

Typically, amino-modified silica supports (1.3 g) were added to 25 mL of anhydrous tetrahydrofuran (THF) and TEA (1 mL) under a nitrogen atmosphere. Then, 2-bromoisobutyryl bromide (0.75 mL) was added dropwise with cooling in an ice–water bath. After 1 h at 0°C, the reaction was allowed to stand at room temperature for 20 h. Thereafter, the products were separated by centrifugation and washed with ethanol. Finally, the silica particles with the ATRP initiators were obtained.

Synthesis of the MIPs by ARGET ATRP

DBT (0.96 mmol), MAA (1.92 mmol), and DVB (14.4 mmol) were added to a Schlenk tube containing toluene (195 mmol). The mixtures were stirred for 1 h, and initiator-modified silica supports (500 mg), Cu(II)Br_2 (0.0062 mmol), and Me_6TREN (0.062 mmol) were added. The tube was deoxygenated by several freeze–pump–thaw cycles. Ascorbic acid (0.062 mmol) was added to the tube, and the tube was immersed in an oil bath, which was thermostated at 30°C, to initiate polymerization. We stopped the polymerization after 24 h by opening the tube and exposing the catalyst to air. The final products were eluted by being thoroughly washed with methanol/acetic acid (9 : 1 v/v) until no template was detectable in the centrifuged supernatant. The novel silica-based core–shell imprinted polymers were obtained after drying at 40°C in a vacuum oven for 48 h. The nonimprinted particles were synthesized under identical conditions but without the template. Meanwhile, other imprinted and nonimprinted polymers (NIPs) were obtained by the same synthetic process.

Adsorption Test

The model solution was prepared by the dissolution of BT, DBT, 4-MDBT, and 4,6-DMDBT in *n*-octane, respectively. According to previous work, the prepared simulated oil had the acidity part as the real oil, and so, the effect of acidity in the solution was not tested.

For adsorption kinetics, to a 10-mL calibrated test tube, 10 mg of adsorbent and 5 mL of DBT model solution (300 mg/L) were subsequently added. The mixture solution was then shaken in the temperature-controlled shaker for different periods of time. The amounts of the residual templates were then quantified with gas chromatography (GC2010, Shimadzu, Japan). We performed equilibrium binding experiments by incubating a given concentration (100–1000 mg/L) of DBT solution (5 mL) with molecularly imprinting polymers coated on the surface of the silica and non-imprinted polymers coated on the surface of the silica 10 mg) in a temperature-controlled shaker. Although the adsorption equilibrium was reached, the tube was taken to determine the concentration of DBT solution.

The batch-mode adsorption kinetic and isotherm studies described previously were conducted at 298, 308, and 318 K, respectively.

We evaluated the binding selectivity by measuring their competitive binding capacities toward DBT and its three kinds of structurally related compounds: SiO_2@MIPs (or SiO_2@NIPs, 10 mg) were incubated with 5 mL of binary mixtures (BT/DBT, 4-MDBT/DBT, and 4,6-DMDBT/DBT) at 318 K. The following processes were basically identical to those of adsorption isotherms.

The adsorption capacities of the adsorbents could be calculated with the following equation:

$$q_t=\frac{(C_0-C_t)V}{m} \quad (2)$$

where q_e and q_t are the amounts of DBT bound to the adsorbent at equilibrium and time t, respectively; C_0, C_e, and C_t are the concentrations of DBT initially, at equilibrium, and at time

Table I. Compositions of the Candidate Prepolymerization Systems (Numbers in Parentheses) and Types of Components Used in These Molecular Dynamic Simulations

Simulation	Template	FM	Crosslinking monomer	Porogen
MD1	DBT (1)	MAA (2)	DVB (5)	Toluene (200)
MD2	DBT (1)	MAA (2)	DVB (15)	Toluene (200)
MD3	DBT (1)	MAA (2)	DVB (25)	Toluene (200)
MD4	DBT (1)	MAA (2)	EDMA (5)	Toluene (200)
MD5	DBT (1)	MAA (2)	EDMA (15)	Toluene (200)
MD6	DBT (1)	MAA (2)	EDMA (25)	Toluene (200)
MD7	DBT (1)	MAA (2)	GDMA (5)	Toluene (200)
MD8	DBT (1)	MAA (2)	GDMA (15)	Toluene (200)
MD9	DBT (1)	MAA (2)	GDMA (25)	Toluene (200)

t, respectively; V is the volume of model solution; and m is the mass of adsorbent added.

The distribution coefficient (K_d), selectivity coefficient (k), and relative selectivity coefficient (k') were defined in eqs. (3–5):

$$K_d = \frac{q_e}{C_e} \tag{3}$$

$$k = \frac{K_d(\mathrm{DBT})}{K_d(\mathrm{analog})} \tag{4}$$

$$k' = \frac{k_{\mathrm{MIP}}}{k_{\mathrm{NIP}}} \tag{5}$$

where C_e is the equilibrium concentration of BT, DBT, 4-MDBT, and 4,6-DMDBT; K_d(template) and K_d(analog) are distribution coefficients of the template and the analog; and k_{MIP} and k_{NIP} are the selectivity coefficients of the SiO_2@MIPs and SiO_2@NIPs toward the template.

Desorption and Repeated Use

A methanol and acetic acid (90 mL/10 mL) mixture was used as the desorption solvent to elute DBT bound to the SiO_2@-MIPs. The regenerated adsorbents were reused for the next adsorption experiment. The adsorption–desorption cycles were implemented five times under the same conditions.

Application of the Adsorbents for a Real Sample

Fluid catalytic cracking gasoline was used to demonstrate the industrial applicability of the as-prepared adsorbent for the deep removal of sulfur. Briefly, the total sulfur content of FCC gasoline was first determined by a Coulomb integrated microanalyzer. An amount 200 mg of SiO_2@MIP was immerged with 5 mL of FCC gasoline under the optimal adsorption conditions until the adsorption was finished. Next, the residual sulfur in the suspension was detected by a Coulomb integrated microanalyzer.

RESULTS AND DISCUSSION

Design of the Optimal MIPs

Molecular Dynamic Simulations of the Prepolymerization Mixtures. Our earlier RHF method specifically targeted computation of the energy of interactions between DBT and several monomers (4VP, Acrylamide, and MAA).[53] In doing so, RHF identified the optimal FM (MAA) capable of forming nonclassical hydrogen bonding interactions with the template DBT. In this instance the optimum proportion for the preassembled complexes was 1 : 2 (DBT/MAA). It is important to note that this model did not account for the influence of the other components present in the prepolymerization mixture, such as CL and solvent. To gain a better insight into the differences and similarities of the interactions between T and FM in the presence of different CLs and thus an optimum design of molecular-imprinting protocols, we used molecular dynamics simulations to investigate the MIP synthesis of the prepolymerization clusters. Three kinds of commercial CLs were selected in terms of the number of double bonds, namely, DVB, EDMA, and GDMA. Details regarding the analyzed atoms are shown in Figure 1. The average spatial distributions of all of the prepolymerization components were extracted from the resulting trajectories with RDFs.

T–FM Interactions During MD1–MD3. Our previous research revealed that DH4 and DH6 could potentially interact by nonclassical hydrogen bonds with MO1 where the molar ratio for DBT and MAA was 1 : 2. Although DH4 and DH6 are not typical hydrogen-bond donors, the electron-withdrawing effects of S on DBT led to their higher local charges, which improved the stability of hydrogen bonds. Further evaluation of the DBT interactions with MAA in this study agreed with the simulation results reported previously.[53] Furthermore, because of the symmetry of the DBT molecule, DH4 and DH6 have the basic same nature. So, the focus of the following discussions was in the interaction between DH6 and MO1.

As shown in Figure 2(A), when the DBT/MAA/DVB molar ratio was 1 : 2 : 5, RDF showed a small peak in the density of MO1 at 4.2Å from DH6; this suggested that there was the very weak interaction between them. Prepolymerization mixtures with a small amount of crosslinkers showed a high flexibility, and however, the strength of interactions between DBT and MAA could not guarantee an accumulation of FMs in the vicinity of the template. From the calculated RDFs evaluating the accumulation of MAA around DBT, a sharp first peak in the density of MO 1 2.7 Å from DH6 indicated that hydrogen-bond interactions transpired during MD2. This correlated well with the

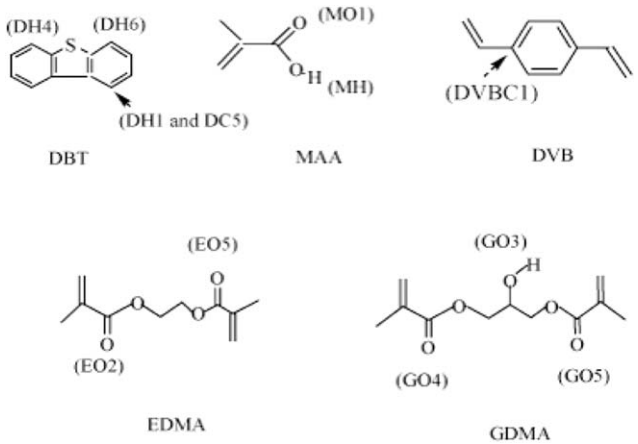

Figure 1. Atoms studied with RDFs.

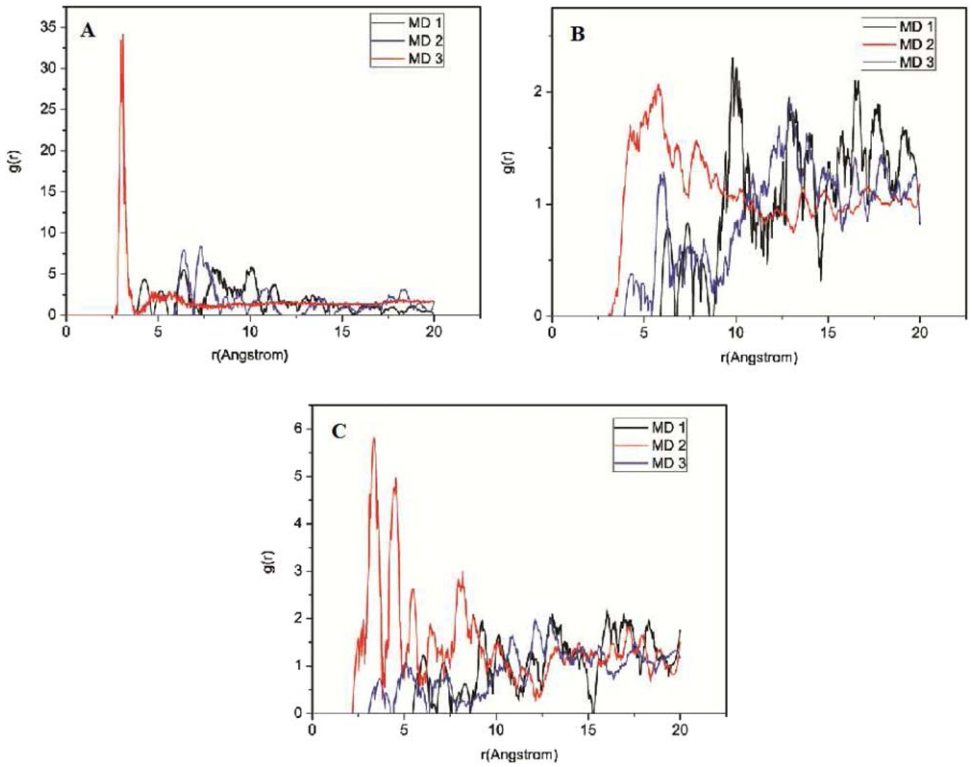

Figure 2. RDFs of (A) MO1–DH6, (B) DVBC1–DC5, and (C) DVBC1–DH1 during MD1–MD3. (g(r) is defined as the ration between the observed number density; r is a certain distance from a solute atom and the average bulk atom). [Color figure can be viewed in the online issue, which is available at wileyonlinelibrary.com.]

observed bond length (2.95684Å) in Gaussian simulation. Although many small peaks in the density of MO1 were also detected between 5 and 20 Å from DH6, the distance to these peaks was much larger than the separation between atoms in a typical noncovalent interaction.[54] Excessive crosslinkers blocked the motion of the FMs, and thus, MAA could not come close to the template. So, there was no specific interaction at a DBT/MAA/DVB molar ratio of 1 : 2 : 25.

Further investigations of the DBT interactions with DVB also displayed a degree of involvement of DVB in the DBT–MIP prepolymerization clusters during MD2. To examine the existence of the π–π stacking interactions between DBT and DVB, we calculated an RDF between DC5 and DVBC1 during MD 2. The evidence for strong π–π interactions between DC5 and DVBC1 was the appearance of a broad peak within 5 Å in MD2 [Figure 2(B)]. The possibility of the T-shape interaction was enhanced by the electron-drawing group (S) of DBT and the electron-donating group (C═C) of DVB. The presence of a T-shaped configuration was then evident from a sharp first peak in the density of DVBC1 at 3.3 Å from DH1 [Figure 2(C)]. During MD2, we observed that DBT interactions with DVB did not cause the lack of the key DBT–MAA interactions. Olsson *et al.*[55] recently reported that CL–T complexes in combination with FM–T complexes were conducive to the improvement of the selectivity of the resulting MIP. So, this candidate prepolymerization system was expected to be the optimal system for the synthesis of DBT molecularly imprinted polymers. The snapshots of the initial and final configurations of MD 2 are presented in Figure 3. Differing from MD 2, the π–π stacking interactions in MD1 and MD3 were negligible.

T–FM Interactions During MD4–MD6. As shown in Figure 4(A), there was no peak found within 5 Å; this indicated a lack of MAA interactions with DBT. To look for the reasons for this behavior, we calculated the RDF between EO2 and DH6 atoms during MD4–MD6. The interactions between DBT and EDMA ensued in hydrogen-bond configurations by sharp peaks in the density of EO2 2.5 Å from DH6 during MD4–MD5 [Figure 4(B)]. This was attributed to the more polar nature of EDMA compared to that of DVB; this reinforced the interactions of DBT with EDMA and weakened the complexes between DBT and MAA. However, no specific interaction between DBT and EDMA was found in MD6. An explanation for this phenomenon could be found when the MAA–EDMA interactions were taken into account. Hydrogen-bonding interactions of MAA with EDMA during MD6 afforded an RDF with a sharp peak in the density of EO2 1.7 Å from MH [Figure 4(C)]; this greatly influenced the DBT–MAA and DBT–EGDMA interactions. Here, the DBT–MAA clusters were unstable because of the disturbances of the DBT–MAA and MAA–EDMA interactions.

T–FM Interaction During MD7–MD9. In the case of GDMA as crosslinkers, no peak in the density of MO1 was detected within 5 Å from DH6; this indicated a complete lack of specific interactions between DBT and MAA during MD7–MD9 [Figure 5(A)]. We then examined DBT–GDMA interactions by molecular dynamic approaches [Figure 5(B,C)]. During MD 8, small

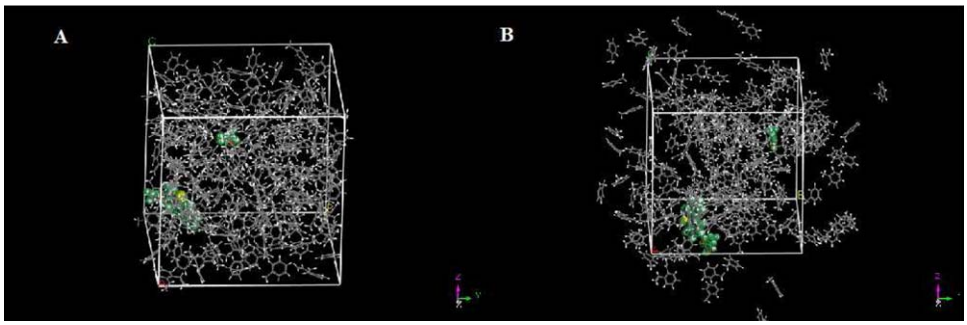

Figure 3. Snapshots of the (A) initial and (B) final configurations of MD2. [Color figure can be viewed in the online issue, which is available at wileyonlinelibrary.com.]

sharp peaks in the density of GO5 4.14 Å and GO3 2.6 Å from DH6 showed the formation of DBT–GDMA complexes. Strong specific interactions between DBT and GDMA in MD 9 transpired; these were verified by small peaks in the density of GO5 3.8 Å and GO3 2.4 Å from DH6. As discussed earlier, FM–CL interactions caused significant disturbances to the nonclassical hydrogen interactions between T and FM. This was evident from the well-defined first peak in the density of GO5 from MH during MD8 [Figure 5(D)]. During MD7 and MD9, there was no strong hydrogen interaction between GO5 and MH. In view of the different molecular structures compared to that of EDMA, GDMA interactions with MAA were further evaluated. As shown in Figure 5(E), the sharp first peak was observed in the density of GO3 1.7 Å from MH during MD7 and MD9. We interpret this result to suggest that the hydrogen-bonding interaction between GO3 and MH severely disrupted the stability of the key T–FM cluster.

As to the previous analysis, DVB was the optimal crosslinker for DBT, and the optimal ratio was 1 : 15 as determined by a comprehensive analysis of the current system. Despite one clear trend that was found upon moving from DVB as crosslinkers to EDMA, Kirsch *et al.*[56] suggested that DVB may be more compatible with the aromatic templates used; thus, this potentially favors ligand recognition in the binding sites and correlates well with our simulation results.

Experimental Verification of the Simulation Results. In this study, nine molecular dynamic simulations were used in an effort to theoretically elucidate the importance of the choice of the crosslinker. Nine kinds of corresponding imprinted and NIPs

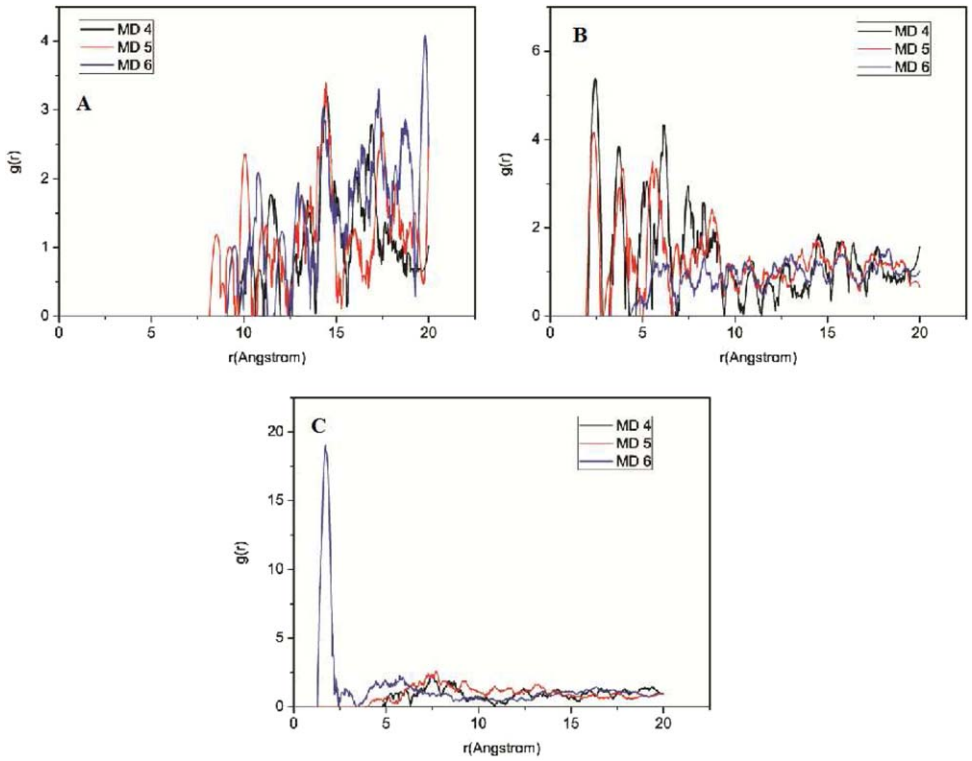

Figure 4. RDFs of (A) DH6–MO1, (B) DH6–EO2, and (C) MH–EO2 during MD4–MD6. (g(r) is defined as the ration between the observed number density; r is a certain distance from a solute atom and the average bulk atom). [Color figure can be viewed in the online issue, which is available at wileyonlinelibrary.com.]

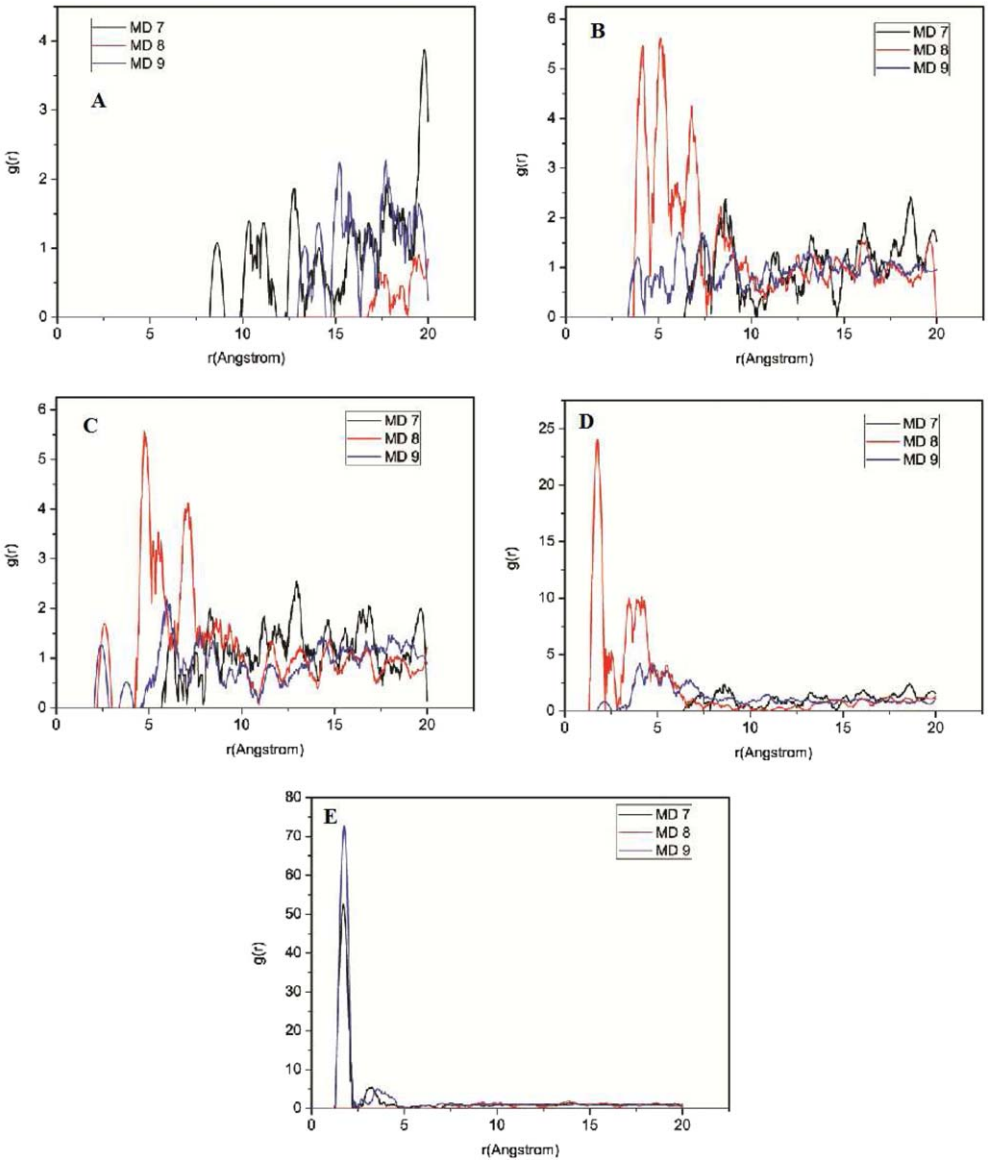

Figure 5. RDFs of (A) DH6–MO1, (B) DH6–GO5, (C) DH6–GO3, (D) MH–GO5, and (E) GO3–MH during MD7–MD9. (g(r) is defined as the ration between the observed number density; r is a certain distance from a solute atom and the average bulk atom). [Color figure can be viewed in the online issue, which is available at wileyonlinelibrary.com.]

were subsequently synthesized to assess the reliability of the molecular dynamics method.

To a 10-mL calibrated test tube, 10 mg of adsorbents and 5 mL of a DBT model solution (300 mg/L) were subsequently added. The mixture was then shaken in the temperature-controlled shaker at 318 K for 12 h. The amounts of residual DBT were then quantified with gas chromatography. The binding percentage (B), K_d, and imprinting factor were used to inspect the binding performances of the adsorbents.[18] The results are shown in Table II. We observed that both the B and imprinting factor values of MD 2 were much higher than those of the other systems; this proved the validity of our design idea. T–FM clusters of MD 2 were the most stable, whereas those of other systems were significantly disturbed by either T–CL interactions or FM–CL interactions. Better binding performances were observed in systems with DVB as CL. Previous studies suggest that the addition of too many FMs generates a large amount of background biding sites with a low affinity and selectivity for the template.[9,16] The role that free uncomplexed CLs play in imprinting processes is just like that excess FMs have played; they increase the number of unselective background binding sites. The deleterious effects caused by free uncomplexed CLs are dependent on the type and concentration of CL. Systems 2, 5, and 8 were selected to investigate the effect of the type of CL. For system 2, DVB potentially made for ligand recognition via additional π–π stacking interactions without an obvious impact on the template interactions with FMs and, thus, efficiently suppressed the formation of background sites. For systems 5 and 8, CLs such as EDMA and GDMA interacted with the FM and had a low affinity for the template DBT; this resulted in a lack

Table II. Binding Parameters of SiO_2@MIP and SiO_2@NIP Prepared with Different Prepolymerization Compositions

System	Polymer	*B* (%)	K_d	Imprinting factor
1	MIP1	8.2857	0.0452	2.2824
	NIP1	3.8074	0.0198	—
2	MIP2	23.1432	0.1506	4.6184
	NIP2	6.1209	0.0326	—
3	MIP3	10.8874	0.0611	2.7174
	NIP3	4.3026	0.0225	—
4	MIP4	7.2923	0.0393	2.0459
	NIP4	3.7023	0.0192	—
5	MIP5	11.9342	0.0678	2.84856
	NIP5	4.5412	0.0238	—
6	MIP6	11.0293	0.0620	2.8257
	NIP6	4.2027	0.0219	—
7	MIP7	7.5432	0.0408	1.9899
	NIP7	3.9386	0.0205	—
8	MIP8	13.7902	0.0799	3.0830
	NIP8	3.6086	0.0259	—
9	MIP9	11.4802	0.0648	2.8644
	NIP9	4.3315	0.0226	—

of DBT interactions with both FM and CL. So, the untemplated sites in systems 5 and 8 took a very big proportion in the as-synthesized imprinted polymers. We selected systems 1, 2, and 3 to investigate the effect of the concentration of CL. For system 1, the low concentration of DVB provided a large space for the molecular movement, and this led to the instability of the intermolecular interactions present in the prepolymerization mixtures. For system 3, excess DVB not only interacted with DBT but also may have hindered the FMs from approaching DBT.

Protocol for Molecular Imprinting at the Surface of the Silica Particles

The schematic route for the preparation of the DBT-imprinted polymers at the surface of the silica nanospheres is shown in Figure 6. Compared with our earlier preparation protocol,[53] the amount of silica particles in the prepolymerization complex was decreased by 50% to prevent the formation of large bulk aggregates. The ATRP initiator layer was deposited on the surface of silica particles; this was followed by the initiation of a living polymerization reaction of organic monomers. According to the simulation results, the nonclassical hydrogen-bonding interactions occurred between MO1 and DH6 (or DH4). This procedure, therefore, yielded a polymer shell with a high density of effective binding sites on the silica surface.

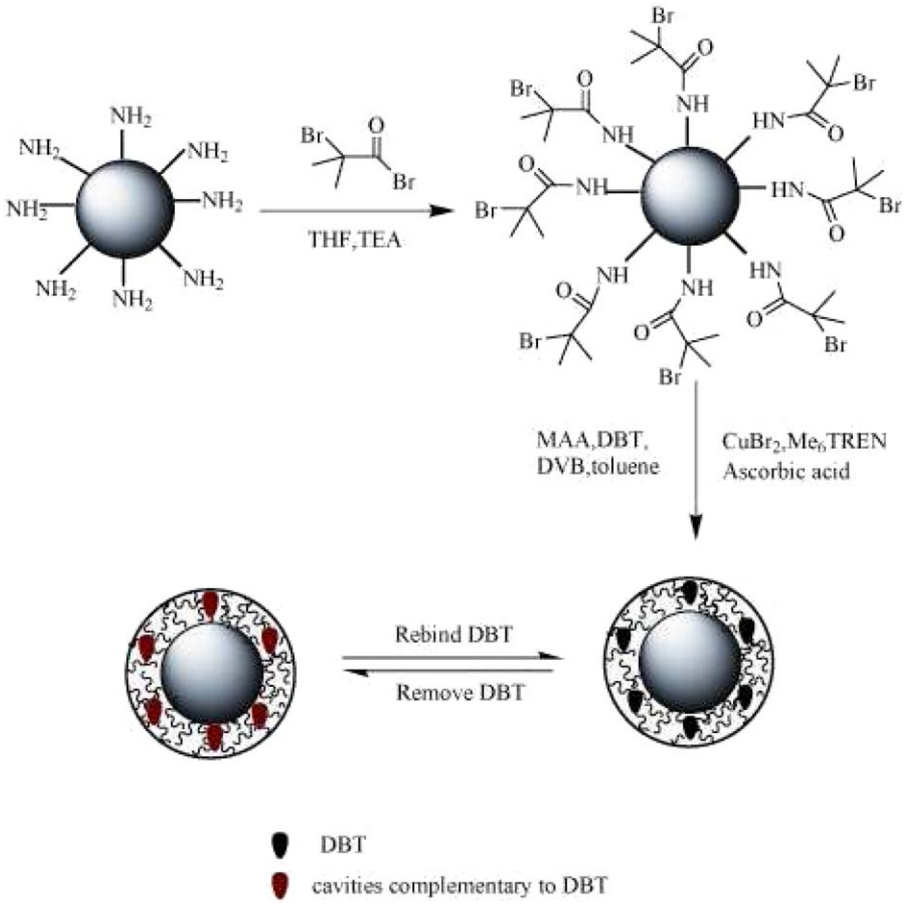

Figure 6. Scheme depicting the fabrication of the imprinted polymer shell. [Color figure can be viewed in the online issue, which is available at wileyonlinelibrary.com.]

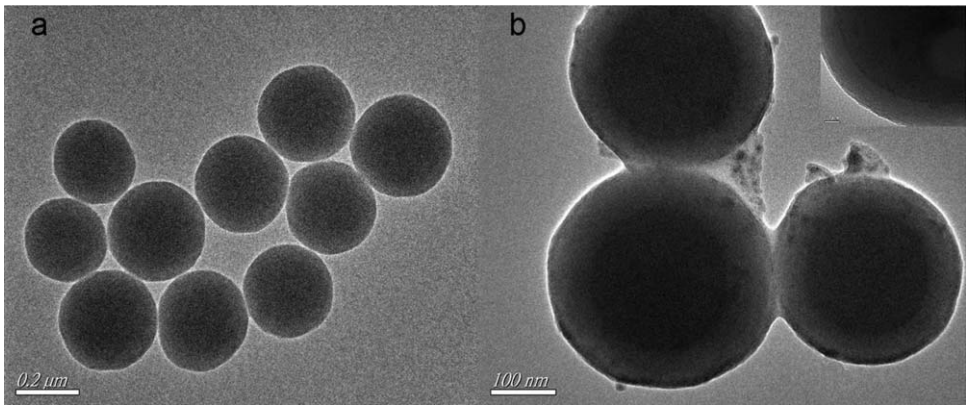

Figure 7. Transmission electron microscopy images of the ATRP initiator-modified silica particles and core–shell imprinted particles.

Characterization of the MIPs and NIPs

Transmission Electron Microscopy Analysis. Transmission electron microscopy images were taken for the initiator-modified silica particles and SiO_2@MIP. As shown in Figure 7, the product was a highly spherical core–shell particle, in which the silica core and imprinting layer on the every particle could be clearly observed. The obtained initiator-modified silica nanospheres were about 250 nm in size. The layer thickness was estimated to be about 40 nm. These facts indicated the successful imprinting of DBT molecules onto the surface of the silica particles.

Nitrogen Adsorption Analysis. The specific area, pore volume, and pore diameter of SiO_2@MIP and SiO_2@NIP particles were calculated by the BET equation and Barrett-Joyer-Halendal model with single-point analysis. The values of these parameters are listed in Table III.

The specific area of SiO_2@MIP was 650.72 m^2/g, whereas that of SiO_2@MIP was 550 m^2/g. The difference in the BET surface area between SiO_2@MIP and SiO_2@NIP may have been due to the cavities created by the imprinting process. The average pore sizes of SiO_2@MIP and SiO_2@NIP measured by the Barrett-Joyer-Halendal pore size distribution were 2.62 and 3.91 nm, respectively, both of which were all mesoporous. Therefore, we concluded that the imprinting process endowed polymer shells with more accessibility to the adsorbate.

IR Spectrum Analysis. In Figure 8, spectral lines a, b, c, and d are the Fourier transform infrared spectra of uniform silica particles, ARGET ATRP initiator-modified silica particles, and SiO_2@MIP, respectively. For spectral line a, the broad and strong peak at 1101 cm^{-1} is the Si—O—Si antisymmetric stretching vibrations. The adsorption peaks found at 473 and 803 cm^{-1} were attributed to the Si—O symmetric bending vibrations and stretching vibration adsorptions, respectively. The Si—OH bending vibrations contributed to the adsorption band at 952 cm^{-1}.

Table III. Pore Properties of SiO_2@MIP and SiO_2@NIP

Sample	Surface area (m^2/g)	Pore volume (cm^3/g)	Pore diameter (nm)
SiO_2@MIP	650.72	1.75	2.62
SiO_2@NIP	550.08	0.32	3.91

The adsorption peak at 3426 cm^{-1} was associated with the —OH asymmetric stretching vibrations of constitution water in the unmodified silica particles. For spectral line b, the success of the formation of an ATRP initiator layer on the silica surface was evident from the appearance of a new broad vibration band at 1674 cm^{-1} corresponding to the characteristic of amide groups. In addition, the appearance of a new adsorption peak at 644 cm^{-1} also demonstrated that SiO_2 was successfully modified by the initiators. For spectral line c, the adsorption band at 3030 and 1450 cm^{-1} represented the =C—H stretching vibrations and C=C stretching vibrations in aromatic nuclei. The C=O stretching vibration adsorption peak appeared at 1733 cm^{-1}. All of these bands proved the successful preparation of the polymer shell on the silica nanoparticles.

Characterization of the Adsorption Performance

Analysis of the Adsorption Kinetics. To clarify the kinetic mechanism of the adsorption process, three kinetic models were used to fit the experimental data.[53]

Figure 9 shows the fitting results for SiO_2@MIP toward DBT and the fitting curves with the pseudo-first-order, pseudo-

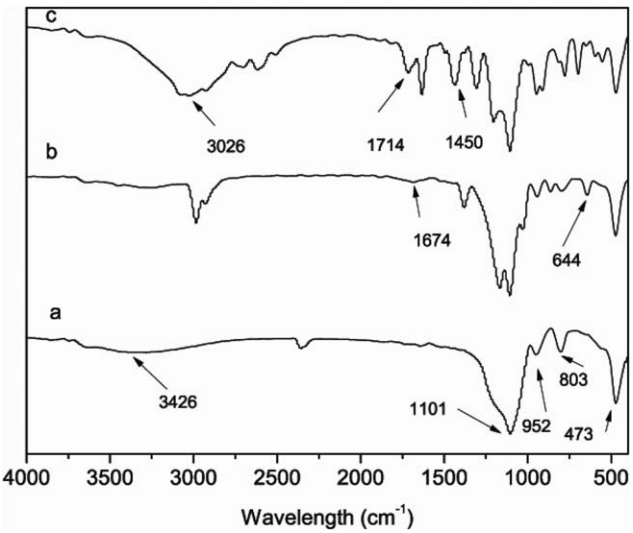

Figure 8. Fourier transform infrared spectra of the (a) silica particles, (b) ATRP initiator-modified silica particles, and (c) core–shell imprinted particles.

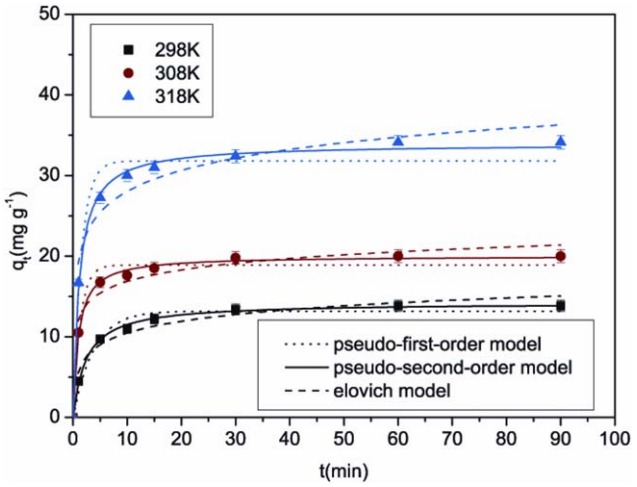

Figure 9. Kinetic adsorption curves of the core–shell imprinted particles at different temperatures. [Color figure can be viewed in the online issue, which is available at wileyonlinelibrary.com.]

second-order, and Elovich models. In the initial several minutes, the binding rate was rapid because of the large quantity of cavities existing on the surface of the polymer shells. Then, the adsorption rate increased slowly until the equilibrium was reached. By contrast with the MIP synthesized in our previous study, which spent a lot of time achieving the equilibrium, this core–shell nanoparticle achieved equilibrium in 30 min; this benefited from the thin polymer shell. We found that SiO_2@-MIP exhibited a higher affinity for DBT than SiO_2@NIP; this was attributed to the imprinting effect. The binding amounts had an obvious positive correlation with temperature; therefore, this indicated the endothermic nature of the adsorption.

The binding kinetic constants determined from the three models with nonlinear regression were listed in Table IV. The related coefficients obtained from the pseudo-second-order model were accordingly larger than those obtained from pseudo-first-order and Elovich models at different temperatures; this was true of both SiO_2@MIP and SiO_2@NIP. Interestingly, in reference, the Elovich model was more suitable for describing the binding process for SiO_2@MIP than the pseudo-second-order model was.[53] We thought that this might have been caused by the macro structure differences in the nanoparticles and different microscopic constituents of the imprinting shells.

Analysis of Adsorption Diffusion. For a general liquid–solid adsorption process, the film diffusion and interparticle diffusion are the dominant interactions. To investigate the influence of the film and intraparticle diffusion, the film diffusion mass-transfer rate equation and Dunwald–Wagner intraparticle diffusion model were applied to analyze the experimental data.[53]

The linear regression plots of $\ln(1 - q_t/q_e)$ versus t for the film diffusion mass transfer of SiO_2@MIP at different temperatures are shown in Figure 10(A). Theoretically, when the plot of $\ln(1 - q_t/q_e)$ versus t is a straight line, one can conclude that the film diffusion is a rate-limiting step. When it came to the analyses of the intraparticle diffusion effect of SiO_2@MIP at different temperatures, a similar conclusion could be drawn [Figure 10(B)]. The parameters obtained from diffusion models with linear regression are reported in Table V. For both the film diffusion mass-transfer rate equation and Dunwald–Wagner intraparticle diffusion model, the constants of SiO_2@MIP were accordingly higher than those of SiO_2@NIP. This indicated that the liquid–solid adsorption interaction was affected by the imprinting process to some extent. As illustrated in Table V, during the adsorption process, both the film and intraparticle diffusion were rate-limiting steps for the imprinted particles, whereas the film diffusion was the major rate-limiting step for the nonimprinted particles.

Analysis of the Adsorption Isotherms. The nonlinear regression curves of the three isotherm models for SiO_2@MIP are shown in [Figure 11(A–C)], and the correlation index constants are listed in Table VI. The highest regression coefficient of the Langmuir model at different temperatures suggested that the Langmuir adsorption model was more relevant than the two others models to the experimental data; this was significantly different from previous studies. In reference work, the Freundlich or Sips isotherm model preferably interpreted the adsorption process of DBT on the imprinted polymers.[53,57] There might have been two factors leading to this distinct result:

Table IV. Kinetic Parameters for the Adsorption Process of SiO_2@MIP and SiO_2@NIP

		SiO_2@MIP			SiO_2@NIP		
Kinetic model		298 K	308 K	318 K	298 K	308 K	318 K
Pseudo-first-order	$q_{e,exp}$ (mg/g)	13.85	20.48	34.03	5.8	6.8	9.2
	$q_{e,calcd}$ (mg/g)	12.8	19.3	33.5	5.4	6.3	8.5
	k_1 (min^{-1})	0.27	0.76	0.67	0.83	0.82	0.75
	R^2 (nonlinear)	0.963	0.971	0.967	0.957	0.945	0.932
Pseudo-second-order	$q_{e,calcd}$ (mg/g)	14.2	20.0	33.9	5.7	6.7	9.1
	k_2 (mg g^{-1} min^{-1})	0.03	0.05	0.02	0.19	0.16	0.11
	R^2 (nonlinear)	0.997	0.989	0.993	0.990	0.997	0.983
Elovich	a (mg g^{-1} min^{-1})	31.59	766.6	663.7	254.4	264.6	241.7
	b (g/mg)	0.48	0.49	0.267	1.72	1.45	1.03
	R^2 (nonlinear)	0.927	0.932	0.924	0.953	0.931	0.925

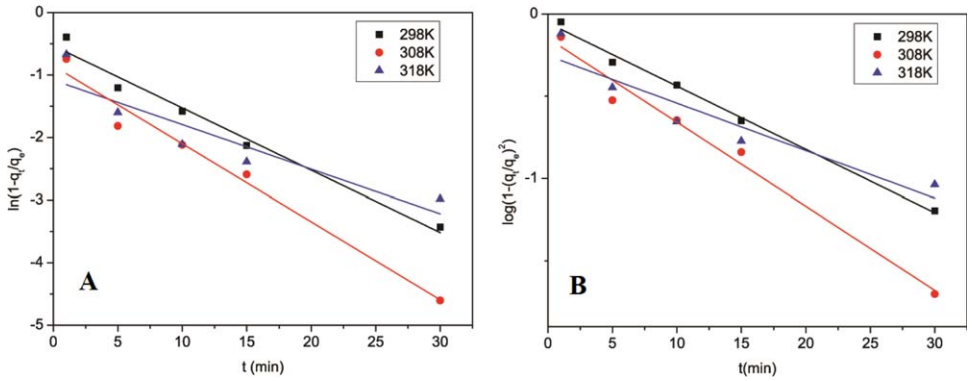

Figure 10. (A) Pore diffusion fitting lines of the core–shell imprinted particles by the film diffusion mass-transfer equation at different temperatures and (B) pore diffusion fitting lines of the core–shell imprinted particles by the Dunwald–Wagner intraparticle diffusion model at different temperatures. [Color figure can be viewed in the online issue, which is available at wileyonlinelibrary.com.]

1. By molecular dynamic simulations, strong EDMA interactions with DBT could be seen to affect the key T–FM complexes formed in the prepolymerization mixtures. When EDMA was chosen as the CL to fabricate DBT-imprinted polymers, it worked like the FM due to strong EDMA interactions with DBT. Therefore, the use of EDMA to prepare DBT-imprinted polymers generated a high percentage of background binding sites in analogy to the excess usage of MAA; this brought about the heterogeneity observed in MIPs. In this study, we replaced EDMA with DVB on the basis of molecular simulation results.
2. The uniform imprinting shell was obtained by a combination of the surface-initiated ARGET ATRP with hierarchical-imprinting technology. Moreover, the good linear curve fitting of a single-site Langmuir-type binding isotherm for SiO_2@-MIP was illustrated in inset with a Scatchard plot equation. The equilibrium K_d values were 1000, 1111, and 769 mg/L at 298, 308, and 318 K, respectively. Accordingly, the maximum numbers of binding cavities were calculated to be 59.8, 99.3, and 130 mg/g. The Scatchard analyses were consistent with the results obtained from the Langmuir nonlinear model.

Analysis of Adsorption Thermodynamics. To understand the effect of the temperature on the adsorption phenomenon, three thermodynamic parameters were introduced. They were standard free energy change (ΔG^0), standard enthalpy change (ΔH^0), and standard entropy change (ΔS^0). The adsorption thermodynamic parameters of SiO_2@MIP are listed in Table VII. The spontaneous peculiarities of the adsorption process at different temperatures were demonstrated by the negative values of ΔG^0. Furthermore, ΔG^0 values increased as the temperature dropped; this indicated that the increase in the temperature was favorable for the adsorption. The positive value of ΔH^0 showed that the adsorption process was endothermic. The entropy-driven natures of the adsorption were also revealed from the positive values of ΔS^0.

Analysis of Selective Adsorption. BT, 4-MDBT, and 4,6-DMDBT were used as potential interferents to study the selectivity of SiO_2@MIP for DBT [Figure 12(A)]. As shown in Figure 12(B), the binding capacities of BT, DBT, 4-MDBT, and 4,6-DMDBT onto SiO_2@MIP were 35.9, 188, 25.2, and 40.7 μmol/g, respectively. The binding capacity of SiO_2@MIP toward the template DBT was greatly improved by molecular imprinting, whereas that of the other analogs just increased a little. To further investigate the selectivity properties, selective and competitive experiments on SiO_2@MIP and SiO_2@NIP were conducted in a dual-solute system. The values of K_d, k, and k' are summarized in Table VIII, and the analysis results are also visualized in Figure 12(C). We obtained the following results from the data in Table VIII:

1. The values of K_d and k of SiO_2@MIP outclassed those of SiO_2@NIP; this indicated that SiO_2@MIP had the best selectivity toward DBT.
2. The values of k' for the analogs increased in rank order from 4-MDBT (4.8008) < BT (5.6397) < 4,6-DMDBT (6.1928).

Table V. Pore Diffusion Coefficients of SiO_2@MIP and SiO_2@NIP at Different Temperatures

		Film diffusion mass-transfer rate equation		Dunwald–Wagner intraparticle diffusion model	
Polymer	Temperature (K)	R'	R^2	k	R^2
SiO_2@MIP	298	0.099	0.972	0.089	0.992
	308	0.071	0.852	0.118	0.976
	318	0.125	0.969	0.066	0.844
SiO_2@NIP	298	0.089	0.920	0.083	0.942
	308	0.065	0.834	0.069	0.862
	318	0.077	0.874	0.062	0.905

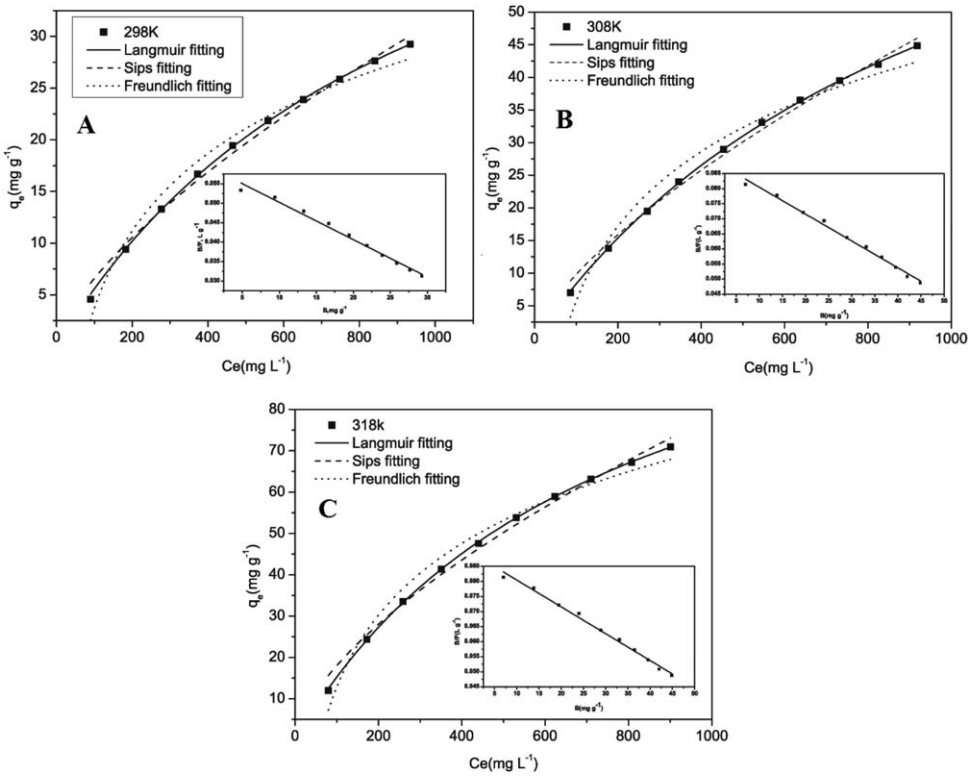

Figure 11. Binding isotherms and fitting curves of the core–shell imprinted particles at (A) 298, (B) 308, and (C) 318 K. The inset shows a Scatchard analysis of the binding capacity of DBT to the core–shell imprinted particles.

Compared with other studies,[28,29,37–46,53,57] the binding selectivity of SiO_2@MIP toward DBT was significantly enhanced.

There were three possible explanations that led to the excellent selectivity for SiO_2@MIP over other antibiotics. In the first case, the Gaussian 09 software package was used to model binding interactions between the target molecules and the FM (MAA) according to the previous reported method.[19–21] The interaction energies (ΔEs) derived from Gaussian simulations are listed in Table IX. ΔEs with MAA increased in rank order from 4-MDBT < BT < DBT < 4,6-DMDBT. DBT and 4,6-DMDBT interacted most strongly with the polymeric chains of the functional units. However, the methyl group on the two sides of the molecular plane may have hindered 4,6-DMDBT from accessing the surface of the adsorbents. Therefore, SiO_2@NIP exhibited higher binding capacities for DBT than for the remaining three analogs. The hypothesis that the imprinting effect of MIP was significantly positively related to the binding properties of the corresponding NIP was proposed and confirmed by Baggiani's group; this was consistent with our results.[58] Second, it was in the procedure of preparing SiO_2@MIP that cavities whose size and structures were matched to DBT formed. DBT's analogs could not enter the cavities easily either because of the oversize molecular volume or because they could not combine steadily with functional groups in the cavities. Third, our synthetic strategy in this study reduced the number of background sites in the imprinting shell of SiO_2@-MIP and thus elevated the selectivity to a high level.

Table VI. Adsorption Isothermal Parameters of SiO_2@MIP toward DBT

Isotherm model		SiO2@MIP		
		298 K	308 K	318 K
Langmuir	K_L (L/mg)	0.00103	9.5×10^{-4}	0.00133
	q_{mL} (mg/g)	59.68	96.14	130.19
	R^2 (nonlinear)	0.998	0.992	0.993
Freundlich	K_{Fl}	0.287	0.395	0.959
	n_F	1.470	1.434	1.570
	R^2 (nonlinear)	0.874	0.891	0.885
Sips	q_{ms} (mg/g)	70.31	120.45	157.56
	a_s	0.00304	0.0031	0.0027
	n_s	0.7514	0.7341	0.7218
	R^2 (nonlinear)	0.965	0.972	0.969

Desorption and Reusability

The reusability for SiO_2@MIP was investigated by five repeated testings of its adsorption capacities to DBT in the adsorption–

Table VII. Thermodynamic Parameters for the Adsorption Process of SiO_2@MIP

Temperature (K)	K_d (mL/g)	ΔG^0 (kJ/mol)	ΔH^0 (kJ/mol)	ΔS^0 (J mol^{-1} K^{-1})
298	28.1	−8.26	35.38	146.5
308	44.4	−9.39	35.38	146.5
318	69.0	−10.49	35.38	146.5

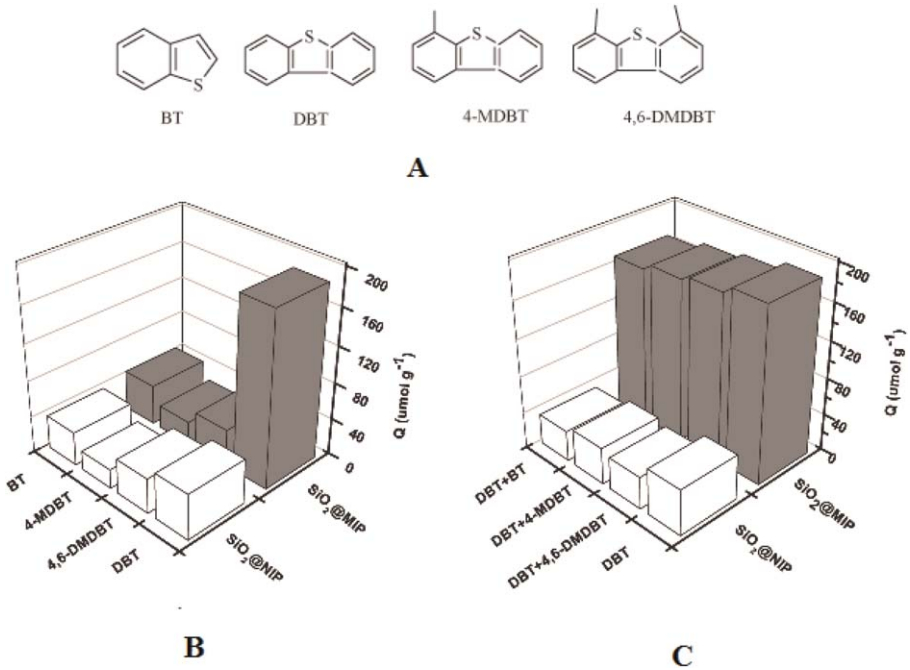

Figure 12. (A) Chemical structures of DBT and its analogs, (B) selective adsorption performance of the core–shell imprinted particles toward DBT (single-solute solution), and (C) selective adsorption performance of core–shell imprinted particles toward DBT (dual-solute solution in the presence of analogs).

Table VIII. Selective Recognition Parameters of SiO_2@MIP and SiO_2@NIP

		SiO_2@MIP		SiO_2@NIP		
Mixed solution	Compound	K_d	k	K_d	k	k'
BT/DBT	DBT	0.1300	—	0.0213	—	—
	BT	0.0158	8.2278	0.0146	1.4589	5.6397
DBT/4-MDBT	DBT	0.1369	—	0.0258	—	—
	4-MDBT	0.0126	10.8651	0.0114	2.2631	4.8008
DBT/4,6-DMDBT	DBT	0.1420	—	0.0225	—	—
	4,6-DMDBT	0.0107	13.2710	0.0105	2.1428	6.1928

desorption procedure, and the results are presented in Figure 13. After five cycles, the adsorption capacity of SiO_2@MIP toward DBT decreased by 11.89% in the DBT solution and by 15.71% in the mixed solution of BT, DBT, 4-MDBT, and 4,6-DMDBT. It was reasonable to assume that SiO_2@MIP could be used repeatedly at least five times without a significant loss in the adsorption capacity.

Analysis of DBT in FCC Gasoline

To verify the feasibility of applying SiO_2@MIP in real samples, FCC gasoline containing 290.91 mg/L sulfur was detected. The sulfur content was decreased to 191.27 mg/L after the first

Table IX. ΔEs between MAA and Benzothiophenes

	ΔE (kJ/mol)			
	BT	DBT	4-MDBT	4,6-DMDBT
MAA	−14.24	−15.70	−6.45873	−15.83

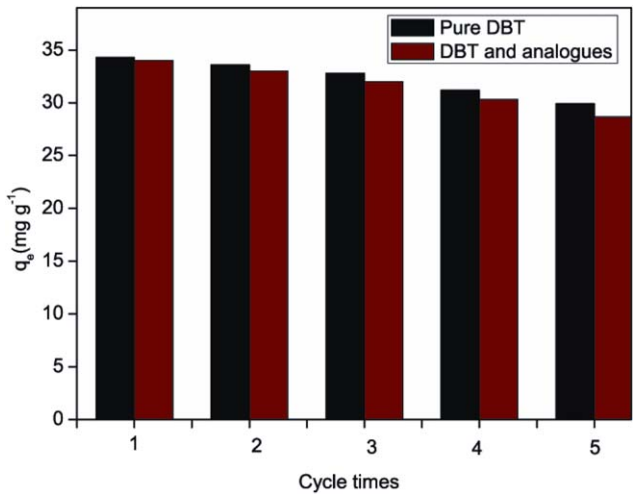

Figure 13. Reusability of the core–shell imprinted particles in a pure DBT solution and a mixture composed of BT, DBT, 4-MDBT, and 4,6-DMDBT. [Color figure can be viewed in the online issue, which is available at wileyonlinelibrary.com.]

adsorption; then, the same operation was conducted again, and the sulfur content was reduced to 125.3 mg/L. These results imply that SiO_2@MIP could be applied to the deep desulfurization of FCC gasoline.

CONCLUSIONS

Through molecular dynamics simulations, we found that the template–FM interactions were simultaneously affected by the type and ratio of T–CL. The optimal crosslinker for DBT imprinting was DVB, and the best ratio between DBT and DVB was 1 : 15. The homogeneous distribution of binding sites and the enhanced selectivity suggested that the main problems faced by the DBT-imprinted polymers were successfully addressed. The results of real sample applications indicated that such SiO_2@MIP nanoparticles are highly promising alternatives to conventional desulfurization technologies in the deep desulfurization field.

ACKNOWLEDGMENTS

This work was subsidized by the National Natural Science Fund (contract grant numbers 21106056 and 21346004), the Jiangsu Natural Science Fund of China (contract grant numbers BK2011512 and BK2014287), the Senior Talent Foundation of Jiangsu University (contract grant number 14JDG057), the Postdoctoral Science Foundation of China (contract grant number 1401012A), and the Research Fund for the Doctoral Program of Higher Education of China (contract grant number 20133227110022).

REFERENCES

1. Hiroyuki, A.; Takayuki, H.; Makoto, K. *Adv. Mater.* **2000**, *12*, 1019.
2. Vlatakis, G.; Andersson, L. I.; Muller, R.; Mosbach, K. *Nature* **1993**, *361*, 645.
3. Awino, J. K.; Zhao, Y. *J. Am. Chem. Soc.* **2013**, *135*, 12552.
4. Dai, J. D.; Zhou, Z. P.; Zou, Y. L.; Wei, X.; Dai, X. H.; Li, C. X.; Yan, Y. S. *J. Appl. Polym. Sci.* **2014**, *131*, 40854.
5. Wang, J.; Dai, J. D.; Meng, M. J.; Song, Z. L.; Pan, J. M.; Yan, Y. S.; Li, C. X. *J. Appl. Polym. Sci.* **2014**, *131*, 40310.
6. Ying, X. G.; Qi, L. L.; Li, X.; Zhang, W. Y.; Cheng, G. X. *J. Appl. Polym. Sci.* **2013**, *127*, 3898.
7. Nicholls, I. A.; Karlsson, B. C. G.; Olsson, G. D.; Rosengren, A. R. *Ind. Eng. Chem. Res.* **2013**, *52*, 13900.
8. Ivanova-Mitseva, P. K.; Guerreiro, A.; Piletska, E. V.; Whitcombe, M. J.; Zhou, Z. X.; Mitesev, P. A.; Davis, F.; Piletsky, S. A. *Angew. Chem. Int. Ed.* **2012**, *51*, 5196.
9. Zhang, Y. G.; Song, D.; Lanni, L. M.; Shimizu, K. D. *Macromolecules* **2010**, *43*, 6284.
10. Manesiotis, P.; Hall, A. J.; Emgenbroich, M.; Quaglia, M.; Lorenzo, E. D.; Sellergren, B. *Chem. Commun.* **2004**, *20*, 2278.
11. Hall, A. J.; Manesiotis, P.; Emgenbroich, M.; Quaglia, M.; Lorenzi, E. D.; Sellergren, P. *J. Org. Chem.* **2005**, *70*, 1732.
12. Wang, Y. X.; Liu, Q. M.; Rong, F.; Fu, D. G. *Polym. Adv. Technol.* **2012**, *23*, 720.
13. Umpleby, R. J.; Bode, M.; Shimizu, K. D. *Analyst* **2000**, *125*, 1261.
14. Unpleby, R. J.; Rushton, G. T.; Shah, R. N.; Rampey, A. M.; Bradshaw, J. C.; Berch, J. K.; Shimizu, K. D. *Macromolecules* **2001**, *34*, 8446.
15. Sibarian-Vazquez, M.; Spivak, D. A. *J. Am. Chem. Soc.* **2003**, *36*, 5105.
16. Yang, W. M.; Liu, L. K.; Zhou, Z. P.; Qiu, C. X.; Ma, P. F.; Liu, H.; Xu, W. Z. *New J. Chem.* **2013**, *37*, 2758.
17. Niu, D. D.; Zhou, Z. P.; Yang, W. M.; Li, Y.; Xia, L.; Jiang, B.; Xu, W. Z.; Huang, W. H.; Zhu, T. Y. *J. Appl. Polym. Sci.* **2013**, *130*, 2859.
18. Liu, L. K.; Cao, Y.; Ma, P. F.; Qiu, C. X.; Xu, W. Z.; Liu, H.; Huang, W. H. *RSC Adv.* **2014**, *4*, 605.
19. Yilmaz, E.; Mosbach, K.; Haupt, K. *Anal. Commun.* **1999**, *36*, 167.
20. Lubke, C.; Lubke, M.; Whitcombe, M. J.; Vulfson, E. V. *Macromolecules* **2000**, *33*, 5098.
21. Hall, A. J.; Manesiotis, P.; Emgenbroich, M.; Quaglia, M.; Lorenzi, E. D.; Sellergren, B. *J. Org. Chem.* **2005**, *70*, 1732.
22. Halhalli, M. R.; Schillinger, E.; Aureliano, C. S. A.; Sellergren, B. *Chem. Mater.* **2012**, *24*, 2909.
23. Ohno, K.; Morinaga, T.; Koh, K.; Tsujii, Y.; Fukuda; T. *Macromolecules* **2005**, *38*, 2137.
24. Liu, B. H.; Han, M. Y.; Guan, G. J.; Wang, S. H.; Liu, R. Y.; Zhang, Z. P. *J. Phys. Chem. C* **2011**, *115*, 17320.
25. Phutthawong, N.; Maseko, R. B.; Summers, C. A. *Eur. Polym. J.* **2013**, *49*, 1111.
26. Boonpangrak, S.; Prachayasittikul, V.; Bülow, L.; Ye, L. *J. Appl. Polym. Sci.* **2006**, *99*, 1390.
27. Cao, Y.; Liu, L. K.; Xu, W. Z.; Wu, X. Y.; Huang, W. H. *J. Appl. Polym. Sci.* **2014**, *131*, 40473.
28. Yang, W. M.; Liu, L. K.; Zhou, Z. P.; Liu, H.; Xie, B. Z.; Xu, W. Z. *Appl. Surf. Sci.* **2013**, *282*, 809.
29. Liu, L. K.; Yang, W. M.; Xu, W. Z.; Zhou, Z. P.; Liu, H.; Yan, Y. S. *Chin. J. Anal. Chem.* **2014**, *42*, 249.
30. Min, K.; Gao, H. F.; Matyjaszewski, K. *Macromolecules* **2007**, *40*, 1789.
31. Audouin, F.; Larragy, R.; Fox, M.; O'Connor, B.; Heise, A. *Biomacromolecules* **2012**, *13*, 3787.
32. Titirici, M. M.; Hall, A. H.; Sellergren, B. *Chem. Mater.* **2002**, *14*, 21.
33. Whitehurst, D.; Isoda, T.; Machida, I. *Adv. Catal.* **1998**, *42*, 345.
34. Zhang, W.; Xu, K.; Zhang, Q.; Liu, D. L.; Wu, S. Y.; Wu, F. *Ind. End. Chem. Res.* **2010**, *49*, 11760.
35. Zhang, H. X.; Gao, J. J.; Meng, H.; Li, C. X. *Ind. Eng. Chem. Res.* **2012**, *51*, 6658.
36. Calzada, J.; Heras, S.; Alcon, A.; Santos, V. E.; Garcia-Ochoa, F. *Energy Fuels* **2009**, *23*, 5491.
37. Yang, W. M.; Zhou, W.; Xu, W. Z.; Li, H.; Huang, W. H.; Jiang, B.; Zhou, Z. P.; Yan, Y; S. *J. Chem. Eng. Data* **2012**, *57*, 1713.
38. Xu, W. Z.; Zhou, W.; Huang, W. H.; Pan, J. M.; Li, H.; Wu, X. Y.; Yan, Y. S. *Microchim. Acta* **2011**, *175*, 167.

39. Huang, W. H.; Li, H.; Xu, W. Z.; Zhou, W.; Zhou, Z. P.; Yang, W. M. *Adsorption Sci. Technol.* **2012**, *30*, 331.
40. Xu, W. Z.; Zheng, X. D.; Gan, M. Y.; Zhu, W. J.; Zhang, Y. L.; Yan, Y. S. *Adsorption Sci. Technol.* **2013**, *31*, 917.
41. Xu, W. Z.; Zhou, Wei; Bian, L. H.; Huang, W. H.; Wu, X. Y. *J. Sep. Sci.* **2011**, *34*, 1746.
42. Huang, W. H.; Zhou, W.; Xu, W. Z.; Xu, X. J.; Yan, Y. S. *Adsorption Sci. Technol.* **2010**, *28*, 629.
43. Xu, W. Z.; Zhou, W.; Xu, P. P.; Pan, J. M.; Wu, X. Y.; Yan, Y. S. *Chem. Eng. J.* **2011**, *172*, 191.
44. Xu, P. P.; Xu, W. Z.; Zhang, X. J.; Pan, J. M.; Yan, Y. S. *Adsorption Sci. Technol.* **2009**, *27*, 975.
45. Xu, P. P.; Xu, W. Z.; Zhang, X. J.; Yan, Y. S. *Microchim. Acta* **2010**, *171*, 441.
46. Huang, W. H.; Zhou, W.; Xu, W. Z.; Xu, P. P.; Xu, X. J.; Yan, Y. S. *Chin. J. Anal. Chem.* **2011**, *39*, 560.
47. Ciampolini, M.; Nardi, N. *Inorg. Chem.* **1966**, *5*, 41.
48. Essmann, U.; Perera, L.; Berkowitz, M. L.; Darden, T. A.; Kollman, P. A. *J. Am. Chem. Soc.* **1995**, *117*, 4193.
49. Karlsson, B. C. G.; O'Mahony, J.; Karlsson, J. G.; Bengtsson, H.; Eriksson, L. A.; Nicholls, I. A. *J. Am. Chem. Soc.* **2009**, *131*, 13297.
50. Sun, H. *J. Phys. Chem. B* **1998**, *102*, 7338.
51. Pricl, S.; Fermeglia, M. *Chem. Eng. Commun.* **2003**, *190*, 1267.
52. Stöber, W.; Fink, A.; Bohn, E. *J. Colloid Interface Sci.* **1968**, *26*, 62.
53. Yang, W. M.; Liu, L. K.; Zhou, Z. P.; Liu, H.; Xie, B. Z.; Xu, W. Z. *Appl. Surf. Sci.* **2013**, *282*, 809.
54. Cleland, D.; Olsson, G. D.; Karlsson, B. C. G.; Nicholls, I. A.; McCluskey, A. *Org. Biomol. Chem.* **2014**, *12*, 844.
55. Olsson, G. D.; Karlsson, B. C. G.; Shoravi, S.; Wiklander, J. G.; Nicholls, I. A. *J. Mol. Recognit.* **2012**, *25*, 69.
56. Kirsch, N.; Alexander, C.; Lübke, M.; Whitcombe, M. J.; Vulfson, E. N. *Polymer* **2000**, *41*, 5583.
57. Liu, W. F.; Zhao, H. J.; Yang, Y. Z.; Liu, X. G.; Xu, B. S. *Appl. Surf. Sci.* **2013**, 146.
58. Baggiani, C.; Giovannoli, C.; Anfossi, L.; Passini, C.; Baravalle, P.; Giraudi, G. *J. Am. Chem. Soc.* **2012**, *134*, 1513.